Ferromagnetic Exchange in the Ground and $^4A_1$ Excited States of $(Et_4N)_3Fe_2F_9$. A Magnetic and Optical Spectroscopic Study

Ralph Schenker,[†] **Høgni Weihe,**[‡] **and Hans U. Güdel***[,†,§]

Departement für Chemie und Biochemie, Universität Bern, Freiestrasse 3, CH-3000 Bern 9, Switzerland,
and H.C. Ørsted Institutet, Københavns Universitet, Universitetsparken 5,
DK-2100 København Ø, Denmark

Received January 30, 2001

The synthesis, crystal growth, magnetic susceptibility, and polarized optical absorption spectra in the visible and near UV of $(Et_4N)_3Fe_2F_9$ are reported. From single-crystal magnetic susceptibility data and high-resolution absorption spectra in the region of the $^6A_1 \rightarrow {}^4A_1$ spin−flip transition, exchange splittings in the ground and excited states are derived. Ferromagnetic ground and excited state exchange parameters $J_{GS} = -1.55$ cm^{-1} and $J_{ES} = -0.53$ cm^{-1} are determined, respectively, and the relevant orbital contributions to the net exchange are derived from the spectra. The results are compared with those reported earlier for the structurally and electronically analogous $[Mn_2X_9]^{5-}$ pairs in $CsMgX_3$:Mn^{2+} ($X = Cl^-$, Br^-), in which the splittings are antiferromagnetic. This major difference is found to be due to the increased metal charge of Fe^{3+} compared to Mn^{2+}, leading to orbital contraction and thus to a strong decrease of the orbital overlaps and hence the antiferromagnetic interactions.

1. Introduction

The magnetic properties of a large number of compounds containing high-spin Fe^{3+} ions have been investigated. Many of them exhibit extended interactions and behave as antiferromagnets at low temperatures, such as, e.g., the fluorides FeF_3,[1] $AFeF_4$ ($A = K^+$, Rb^+, Cs^+),[2,3] and K_2FeF_5,[4] the chlorides $A_2[FeCl_5(H_2O)]$ ($A = NH_4^+$, K^+, Cs^+),[5,6] the sulfides $KFeS_2$ and $CsFeS_2$,[7] and $FePO_4$,[8] or they behave as ferromagnets such as $FeCl[S_2CN(C_2H_5)_2]$.[9] Currently very active research focuses on the development of molecular-based ferromagnets, which might offer some advantages compared to classical magnetic materials due to their chemical nature. A molecular material is easier to modify, and the magnetic properties could be combined with optical, mechanical, and electrical properties. Another very active field of molecular magnetism deals with spin clusters containing a finite number of paramagnetic ions. This has been triggered by the observation of magnetic hysteresis and quantum tunneling in the complex $[Mn_{12}O_{12}(OAc)_{16}(H_2O)_4]\cdot 2HOAc\cdot 4H_4O$.[10] These clusters behave as nanomagnets and show magnetic bistability at very low temperature. Similar behavior has been reported for a number of clusters, also including the oxygen-bridged Fe^{3+} clusters $[Fe_4(OCH_3)_6(dpm)_6]$ (dpmH = dipivaloylmethane),[11] $[Fe_8O_2(OH)_{12}(tacn)_6]^{8+}$ (tacn = 1,4,7-triazacyclo-nonane),[12] and $[Fe_{10}Na_2\text{-}(O)_6(OH)_4(O_2CPh)_{10}(chp)_6\text{-}(H_2O)_2(Me_2CO)_2]$ (chp = 6-chloro-2-pyridonato).[13,14]

Understanding the magnetic properties of this wide variety of compounds is still a challenging problem, since it requires a detailed knowledge of the underlying exchange interactions between nearest neighbors. In a dimer these can be investigated without the complications arising from the presence of a multitude of interactions between paramagnetic ions in polynuclear clusters. Therefore, investigations of dinuclear complexes, especially those with ferromagnetic coupling, remain an important area of research. A number of Fe^{3+} dimers with oxo bridges were studied.[15] In contrast, only two compounds which contain isolated halido-bridged dimers were magnetically investigated so far. For $Cs_3Fe_2Cl_9$[16] an antiferromagnetic interaction was reported, whereas in $Cs_3Fe_2F_9$ it was found to be ferromagnetic.[17] For the latter, additional antiferromagnetic interdimer exchange interactions were reported.

The various orbital contributions to the total exchange cannot be obtained from an analysis of the ground state properties. Optical spectroscopy of highly resolved transitions is an appropriate technique to determine exchange splittings not only

---

[†] Universität Bern.

[‡] Københavns Universitet.

[§] E-mail: hans-ulrich.guedel@iac.unibe.ch. Fax: +41 31 631 43 99.

(1) Ferey, G.; Varret, F.; Coey, J. M. D. *J. Phys. Chem.* **1979**, *12*, L531.

(2) Heger, G.; Geller, R.; Babel, D. *Solid State Commun.* **1971**, *9*, 335.

(3) de Jongh, L. J.; Miedema, A. R. In *Experiments on Simple Magnetic Model Systems*; Coles, B. R., Ed.; Taylor & Francis Ltd: London, 1974; p 97.

(4) Sabatier, R.; Soubeyroux, J. L.; Dance, J. M.; Tressaud, A.; Winterberger, M.; Fruchart, D. *Solid State Commun.* **1979**, *29*, 383.

(5) O'Connor, J. C.; Deaver, B. S.; Sinn, E. J. *J. Chem. Phys.* **1979**, *70*, 5161.

(6) Palacio, F.; Paduan-Filho, A.; Carlin, R. L. *Phys. Rev. B: Condens. Matter* **1980**, *B21*, 296.

(7) Tiwar, S. K.; Vasudevan, S. *Phys. Rev. B* **1997**, *56*, 7812.

(8) Reiff, W. M. In *Magneto-Structural Correlations in Exchange Coupled Systems*; Willet, R. D., Gatteschi, D., Kahn, O., Eds.; NATO ASI series, D. Reidel Publishing Co.: Dordrecht, 1985; p 355.

(9) Carlin, R. L. *Magnetochemistry*; Springer-Verlag: Berlin, 1986; p 272.

(10) Caneschi, A.; Gatteschi, D.; Sessoli, R.; Barra, A.-L.; Brunel, L.-C.; Guillot, M. *J. Am. Chem. Soc.* **1991**, *113*, 5873.

(11) Barra, A.-L.; Caneschi, A.; Cornia, A.; Fabrizi de Biani, F.; Gatteschi, D.; Sangregoria, C.; Sessoli, R.; Sorace, L. *J. Am. Chem. Soc.* **1999**, *121*, 5302.

(12) Barra, A.-L.; Debrunner, P.; Gatteschi, D.; Schulz, C. E.; Sessoli, R. *Europhys. Lett.* **1995**, *35*, 133.

(13) Benelli, C.; Parsons, S.; Solan, G. A.; Winpenny, R. E. P. *Angew. Chem., Int. Ed. Engl.* **1996**, *35*, 1825.

(14) Benelli, C.; Cano, J.; Journeaux, Y.; Sessoli, R.; Solan, G. A.; Winpenny, R. E. P. *Inorg. Chem.* **2001**, *40*, 188.

(15) Weihe, H.; Güdel, H. U. *J. Am. Chem. Soc.* **1997**, *119*, 6539, and references therein.

(16) Ginsberg, A. P.; Robin, M. B. *Inorg. Chem.* **1963**, *2*, 817.

(17) Dance, J. M.; Mur, J.; Darriet, J.; Hagenmüller, P.; Massa, W.; Kummer, S.; Babel, D. *J. Solid State Commun.* **1986**, *63*, 446.

10.1021/ic010129p CCC: \$20.00

within the ground state but also within excited states, thus allowing one to elucidate the relevant orbital pathways of exchange and therefore the bonding properties between the paramagnetic ions. In d^5 systems the $^6A_1 \rightarrow {}^4A_1$ spin−flip transition is of particular interest, since it often consists of sharp lines and can thus be very informative. Hence, a large number of compounds with the isoelectronic Mn^{2+} ion were investigated by optical spectroscopy in the past.[18−22] A detailed study of the optical spectra of the $^4A_1$ pair transitions in $CsMgX_3:Mn^{2+}$ ($X = Cl^-$, Br^-) containing $[Mn_2X_9]^{5-}$ pairs was reported.[23] In contrast, optical spectroscopic studies of d−d transitions in Fe^{3+} compounds are still scarce in the literature. Antiferromagnetic ground state exchange splittings were derived from pair spectra of Fe^{3+} in natural yellow sapphires[24] as well as in oxo-bridged Fe^{3+} dimers.[25,26]

In this study we present the synthesis and single-crystal growth of the compound $(Et_4N)_3Fe_2F_9$, **1**, in which the $[Fe_2F_9]^{3-}$ dimer is composed of two face-sharing octahedra. This compound is especially suitable for optical spectroscopy due to its high hexagonal symmetry. The hexagonal crystal axis coincides with the trigonal dimer axis. We report polarized optical absorption spectra of single crystals between 12 000 and 45 000 cm^{-1}, as well as single-crystal magnetic susceptibility data. Ferromagnetic exchange splittings in the ground and $^4A_1$ states are derived from high-resolution absorption spectra at cryogenic temperatures. In contrast to the situation in $Cs_3Fe_2F_9$,[17] the dimers are well separated from each other in the title compound due to the bulky Et_4N^+ ions. Interdimer exchange interactions are therefore negligibly weak, which allows us to study the interactions in the $[Fe_2F_9]^{3-}$ complex in the absence of cooperative effects. The knowledge of the excited state splittings allows us to elucidate the role of different orbital exchange pathways in contributing to the observed net ferromagnetic splittings. The results are compared to those reported earlier for analogous dimer compounds such as $CsMgX_3:Mn^{2+}$ ($X = Cl^-$ **2**, Br^- **3**) containing $[Mn_2X_9]^{5-}$ pairs,[23] $Cs_3Fe_2Cl_9$ **4**,[16] and $(Et_4N)_3Cr_2F_9$ **5**.[27] In all of them the triply bridged dimers possess trigonal symmetry.

2. Experimental Section

2.1. Synthesis and Crystal Structure. All the chemicals used for the present study were at least of reagent grade. Being extremely hygroscopic, the title compound was synthesized using Schlenk techniques throughout. A total of 325 mg (2 mmol) of $FeCl_3$ (Cerac, 99.8%) was dissolved in 30 mL of dry DMF. After heating to 80 °C, 7.2 mL (9 mmol) of a 1.25 M dry ethanolic solution of Et_4NF (preparation described previously in ref 27) was added. The solution lost its yellow color almost completely, indicating the formation of the $[Fe_2F_9]^{3-}$ complex. After concentrating to 12 mL, the solution was allowed to cool slowly from 130 °C to room temperature within 48 h. The product with formula $(Et_4N)_3Fe_2F_9$ crystallized in small, completely colorless needles up to 0.5 mm in length. Larger crystals with typically 1 mm thickness and 3−5 mm length were grown by slow diffusion of diethyl ether into a saturated solution of $(Et_4N)_3Fe_2F_9$ in DMF within 5 days, using a crystallization cell with a glass frit. The product was filtered, washed with a minimum amount of dry DMF (3 mL), and dried under vacuum. It is very hygroscopic and decomposes completely within minutes when exposed to air. The crystals were therefore stored and handled in a drybox under a dry nitrogen atmosphere. The purity of the bulk material was checked by powder X-ray diffraction and comparison with the single-crystal structural data of the isomorphous $(Et_4N)_3Cr_2F_9$ compound.[28] $(Et_4N)_3Fe_2F_9$ crystallizes in the hexagonal space group $P6_3/m$, with $a = 13.304$ Å and $c = 10.765$ Å, obtained from a Rietveld analysis on powder X-ray diffraction data at room temperature.[28] The Fe^{3+} single ion and dimer point groups are exactly C_3 and C_{3h}, respectively, with the 3-fold axis lying parallel to the hexagonal crystal c axis. The Fe−Fe distance is 2.864 Å.

2.2. Optical Absorption and Transmission Measurements. Polarized crystal absorption spectra were measured in the spectral range 830−220 nm in both σ and π polarization, i.e., with the electric vector of the light perpendicular and parallel to the c axis, respectively. A hexagonal needle with the dimensions 3.2 mm × 0.64 mm × 0.96 mm was used. Survey absorption spectra in the visible and UV were recorded on a double-beam spectrometer Cary 05e (Varian), and the sample was cooled to 12 K using a closed-cycle helium refrigerator (Air Products). High-resolution transmission spectra $I(\lambda)$ around 400 and 350 nm were performed as single-beam experiments as follows: The light of a 100 W tungsten lamp was dispersed by a 0.85 m double monochromator (Spex 1402), polarized using a pair of Glan-Taylor prisms, focused on the sample, and detected by a cooled PM tube (RCA 31034) in conjunction with a photon counting system (Stanford Research SR 400). Variable sample temperatures between 1.6 and 28 K were achieved using a liquid helium bath cryostat (Oxford Instruments 20 mm Bath Cryostat). A glass filter absorbing in the visible (Schott BK3) was mounted between the sample and the detector to suppress straylight. A mercury lamp was used for wavelength calibration. A background spectrum $I_0(\lambda)$ was detected with removed sample. Absorption spectra were then obtained by calculating $\log(I_0(\lambda)/I(\lambda))$.

2.3. Magnetic Measurements. Variable-temperature magnetic susceptibility measurements were carried out on a single crystal in the temperature range 300−2 K at a magnetic field of 0.1 T using a magnetometer (Quantum Design MPMS-XL-5) equipped with a SQUID sensor. The crystal was sealed in a glass tube and oriented with its hexagonal axis parallel and perpendicular to the magnetic field. The data were corrected for the diamagnetism of the atoms using Pascal's constants.

3. Results

Figure 1 shows the temperature dependence between 1.8 and 50 K of the product χT, where χ is the molar magnetic susceptibility, of single crystals oriented with their hexagonal axis parallel ($H \parallel c$) and perpendicular ($H \perp c$) to a magnetic field of 0.1 T. Above 50 K, χT remains constant at about 10 $cm^3\ K\ mol^{-1}$ for both $H \parallel c$ and $H \perp c$ (not shown). Below 40 K, χT is increasing with decreasing temperature. For $H \parallel c$, χT steadily increases, whereas for $H \perp c$ it goes through a maximum around 5 K.

Overview absorption spectra in π (upper trace) and σ (lower trace) polarizations between 13 000 and 45 000 cm^{-1} at 15 K are shown in Figure 2. The assignment of the principal bands is straightforward from a comparison with Mn^{2+} d−d spectra.[23] Octahedral labels are used although the actual symmetry is trigonal. The inset shows the enlarged $^4T_1(G)$ band in π polarization. It shows indications of two Franck−Condon progressions in a 325 cm^{-1} frequency mode built on origins at 13 450 and 13 630 cm^{-1}.

Figure 3 shows the π (upper graph) and σ (bottom graph) polarized spectra in the region of the $^4A_1$, $^4E(G)$ bands at 1.6 K

---

(18) Ferguson, J.; Guggenheim, H. J.; Tanabe, Y. *J. Phys. Soc. Jpn.* **1966**, *21*, 692.
(19) Day, P.; Dubicki, L. *J. Chem. Soc., Faraday Trans. 2* **1973**, *69*, 363.
(20) Ferguson, J.; Güdel, H. U.; Krausz, E. R.; Guggenheim, H. J. *Mol. Phys.* **1974**, *28*, 893.
(21) Cole, G. M.; Putnik, C. F.; Holt, S. L. *Inorg. Chem.* **1975**, *14*, 2219.
(22) Putnik, C. F.; Cole, G. M.; Holt, S. L. *Inorg. Chem.* **1976**, *15*, 2135.
(23) McCarthy, P. J.; Güdel, H. U. *Inorg. Chem.* **1984**, *23*, 880.
(24) Ferguson, J.; Fielding, P. E. *Aust. J. Chem.* **1972**, *25*, 1371.
(25) Schugar, H. J.; Rossman, G. R.; Barraclough, C. G.; Gray, H. B. *J. Am. Chem. Soc.* **1972**, *94*, 2683.
(26) Brown, C. A.; Remar, G. J.; Musselman, R. L.; Solomon, E. I. *Inorg. Chem.* **1995**, *35*, 688.
(27) Schenker, R.; Heer, S.; Güdel, H. U.; Weihe, H. *Inorg. Chem.* **2001**, *40*, 1482.
(28) Krämer, K. W.; Schenker, R.; Hauser, J.; Weihe, H.; Bürgi, H. B.; Güdel, H. U. *Z. Anorg. Allg. Chem.*, in press.

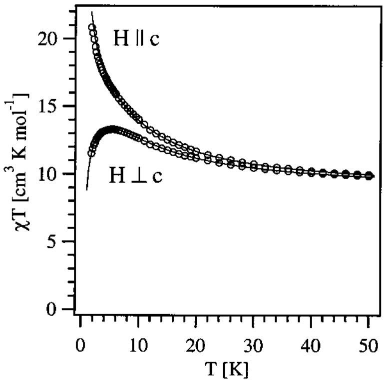

Figure 1. Temperature dependence of the magnetic susceptibility plotted as the product χT of a single crystal of $(Et_4N)_3Fe_2F_9$ in the range 1.8−50 K (circles). The crystal was oriented with its *c* axis parallel ($H \parallel c$) and perpendicular ($H \perp c$) to the magnetic field of 0.1 T. The solid line is a fit with the parameters $J_{GS} = -1.55$ cm^{-1}, $D = -0.15$ cm^{-1}, and *g* fixed at 2.00.

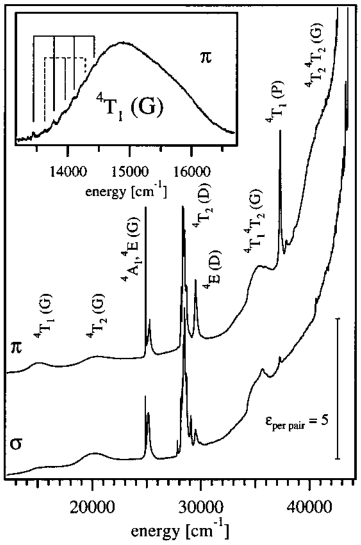

Figure 2. Polarized single-crystal survey absorption spectra of $(Et_4N)_3$-Fe_2F_9 at 15 K. The bands are denoted in *O* symmetry, with the corresponding free-ion terms in parentheses. The inset shows the vibrational progressions built on the origins at 13450 and 13630 cm^{-1} of the $^4T_1(G)$ band in π polarization on an enlarged scale.

(solid lines) and 14.4 K (dotted lines). In both polarizations at 14.4 K the spectra are dominated by a prominent, sharp peak around 24 880 cm^{-1}. Its intensity strongly decreases and its position slightly red-shifts with decreasing temperature in π polarization, whereas it is temperature independent in σ. A broad band extends from 24 800 to 25 500 cm^{-1}, with no temperature dependence in π but increasing intensity upon heating in σ polarization. Superimposed on the broad band, a number of sharp, weak features are observed. The numbers indicate their energy separation from the prominent peak at 24 880 cm^{-1}.

Enlarged high-resolution absorption spectra in the range of the $^6A_1 \rightarrow {}^4A_1$ pair transitions are shown in Figure 4 at various temperatures as indicated. In both polarizations the spectra show a distinct temperature dependence, and the hot intensity is at least an order of magnitude larger in π than in σ polarization. In π polarization at 1.6 K, only one peak is observed at 24 873 cm^{-1}. It is superimposed by a hot band rising with temperature at about the same energy. Upon heating, a prominent band at 24 881 cm^{-1} starts rising. Above 4.2 K it slightly red-shifts, indicating the presence of an additional hot band at about 24 877 cm^{-1}. The σ spectrum is dominated by a single band at 24 873 cm^{-1}, which is essentially temperature independent. At 1.6 K, there is an additional, very weak and broad band between 24 882 and 24 890 cm^{-1}. A hot band rises at 24 881 cm^{-1}, and at 14.4 K there is an indication of a shoulder on the high-energy side of the cold band at about 24 877 cm^{-1}. Table 1 lists the energies, polarizations, intensities, and temperatures of the bands.

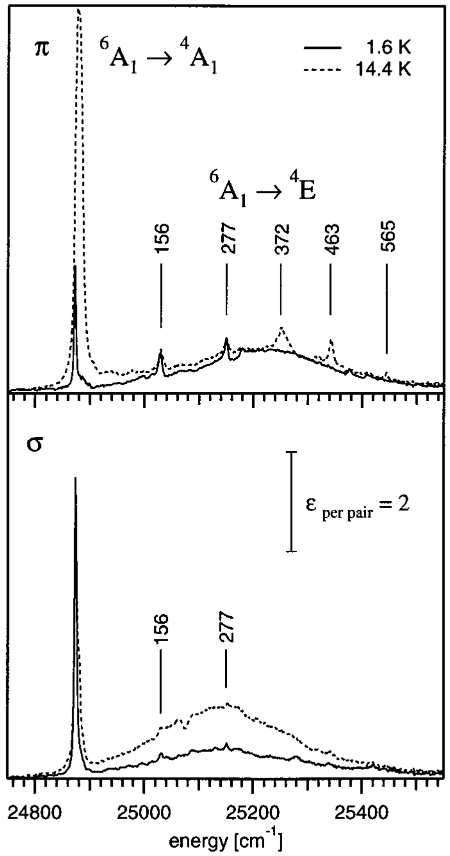

Figure 3. π (upper graph) and σ (bottom graph) polarized absorption spectra in the region of the $^6A_1 \rightarrow {}^4A_1$, ^4E transitions at 1.6 (solid lines) and 14.4 K (dotted lines). Sidebands are denoted with their energy separations from the strong origin lines.

Figure 5 shows enlarged high-resolution absorption spectra in the range of the $^6A_1 \rightarrow {}^4T_2(D)$ transition in π (solid line) and σ (dotted line) polarizations at 1.6 K. The spectra are divided into three regions, region I covering the range below 28 170 cm^{-1}, region II from 28 170 to 28 400 cm^{-1}, and region III above 28 400 cm^{-1}, as indicated at the top of Figure 5. In both regions II and III, the spectra are essentially cold. Region II is dominated by two sharp, prominent peaks labeled 8 and 9 at 28 290 and 28 360 cm^{-1}, respectively, which are more intense in π than in σ polarization. Region III consists of several weaker bands which are assigned to vibrational sidebands, forming short progressions built on the origins in the regions I and II, as indicated by the bars in Figure 5. The vibrational frequencies range from 280 to 323 cm^{-1}, i.e., similar to the 325 cm^{-1} mode forming progressions in the $^4T_1(G)$ band, see Figure 2. Additional modes may contribute to the unresolved intensity in region III. Nine origin bands are observed in regions I and II, labeled 1−9 in Figure 5. The σ (top graph) and π (bottom graph) polarized spectra of region I are shown on an enlarged scale in Figure 6 at various temperatures between 1.6 and 28.5 K as indicated. We label corresponding cold and hot bands with the same numbers and distinguish them by the indices a and b, respectively. Six cold bands numbered from 1a to 5a and 6 in Figure 6 are observed in σ polarization, but only bands 4a and

Table 1. Energies (cm^{-1}), Polarizations, Temperatures (K), Oscillator Strengths (*f*), and Assignment (in C_{3h}) of the Observed $^6A_1 \rightarrow {}^4A_1$ Pair Transitions in $(Et_4N)_3Fe_3F_9$, See Figure 4[a]

energy					
exp	calcd	polarizn	temp	*f*	assignment
24 873	24 873	π/σ	1.6	$1.3 \times 10^{-8}/4.1 \times 10^{-8}$	$^{11}A'' \rightarrow {}^9A'$
24 873	24 873	π	2.3		$^9A' \rightarrow {}^7A''$
24 877	24 877	π/σ	7.8		$^7A'' \rightarrow {}^7A'$
24 881	24 881	π/σ	2.3/4.2	$5.6 \times 10^{-8}/2.9 \times 10^{-8}$	$^9A' \rightarrow {}^9A''$
24 882−24 890	24 888	π/σ	1.6	$\approx 1 \times 10^{-9}$	$^{11}A'' \rightarrow {}^9A''$

[a] The calculated energies are listed in the third column. The lowest temperature at which a given transition is observed is indicated.

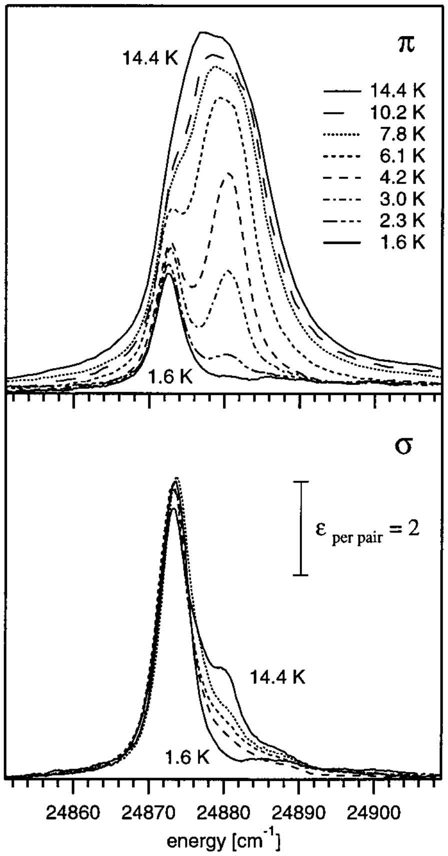

Figure 4. High-resolution absorption spectra showing the temperature dependence of the $^6A_1 \rightarrow {}^4A_1$ pair transitions in π (top graph) and σ (bottom graph) polarizations at various temperatures between 1.6 and 14.4 K as indicated.

6 appear in π polarization. Hot, exclusively π polarized bands arise upon heating, labeled 1b−5b in Figure 6. Energies, polarizations, and temperatures of cold and hot bands 1−9 are shown in Table 2.

4. Analysis

4.1. Magnetic Properties. The ground state exchange splittings are described in terms of the isotropic Heisenberg Hamiltonian

$$H = J_{GS}(S_A \cdot S_B) \tag{1}$$

with $S_A = S_B = {}^5/_2$, where a negative value for the exchange parameter J_{GS} corresponds to a ferromagnetic splitting. The differences in the susceptibility curves for the $H \parallel c$ and $H \perp c$ orientations below 40 K were rationalized with an axial zero-field splitting (ZFS) at the Fe^{3+} site parametrized by *D*. The magnetic susceptibility was then calculated using the program ANIMAG based on the formalism presented in ref 29. With

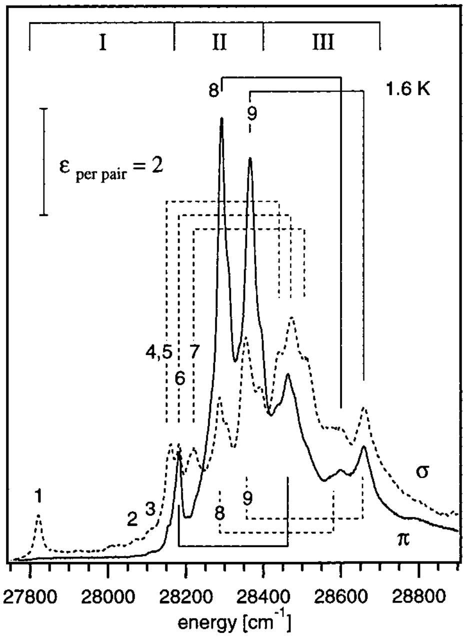

Figure 5. π (solid line) and σ (dotted line) polarized absorption spectra in the region of the $^6A_1 \rightarrow {}^4T_2$ (D) transition at 1.6 K. The solid and dotted bars indicate vibrational progressions in π and σ polarizations, respectively. The numbers label the electronic transitions.

the parameter values $J_{GS} = -1.55$ cm^{-1}, $D = -0.15$ cm^{-1}, and *g* fixed at 2.00 the experimental data are very well reproduced, see Figure 1. The ground state exchange splitting is thus ferromagnetic, giving rise to a Landé pattern with the $S = 5$ level lying lowest and an energy separation between the $S = 5$ and $S = 4$ levels of $5|J_{GS}| = 7.75$ cm^{-1}. In $Cs_3Fe_2F_9$, a value $J_{GS} = -1.36$ cm^{-1} was derived from magnetic susceptibility measured on a powder sample.[17] Instead of axial anisotropy, antiferromagnetic interdimer interactions were introduced to account for the observed drop of below 20 K. In $(Et_4N)_3Fe_2F_9$, there is no evidence for interdimer interactions, and they are much more unlikely, since the dimers are well separated from each other due to the bulky Et_4N^+ ions. The single-crystal data allow an unambiguous determination of the sign of the single-ion axial anisotropy parameter *D*, which is not possible from data obtained from powder samples. The total ZFS of a given dimer spin level *S* is given by $|D_S|S^2$, where the dimer D_S is related to the single-ion *D*, and for $S = 5$ $D_{S=5} = {}^4/_9 D$.[30] For the dimer ground level we thus get $D_{S=5} = -0.066$ cm^{-1} and a total ZFS of 1.66 cm^{-1}. This is considerably smaller than the 7.75 cm^{-1} exchange splitting between the $S = 5$ and $S = 4$ levels. In the optical spectra the ZFS is not resolved and will be ignored in the following analysis.

---

(29) Borrás-Almenar, J. J.; Clemente-Juan, J. M.; Coronado, E.; Tsukerblat, B. S. *Inorg. Chem.* **1999**, *38*, 6081.

(30) Kahn, O. *Molecular Magnetism*; VCH Publishers: New York, 1993; p 142.

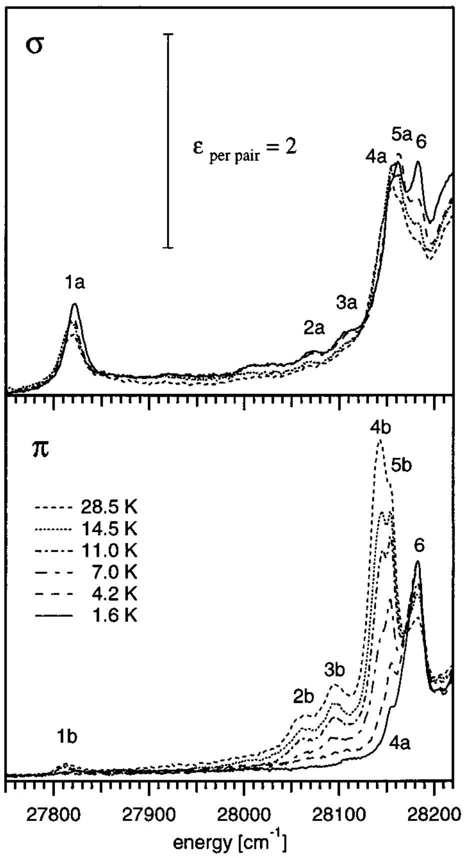

Figure 6. σ (upper graph) and π (bottom graph) polarized absorption spectra of the lowest bands of the ${}^6A_1 \rightarrow {}^4T_2$ (D) transition shown in Figure 5 at various temperatures between 1.6 and 28 K as indicated. The observed bands are labeled from 1 to 6, with a and b designating cold and hot bands, respectively.

Table 2. Energies (cm^{-1}), Polarizations, Temperatures (K), Oscillator Strengths (*f*), and Assignment of the ${}^6A_1 \rightarrow {}^4T_2(D)/{}'^2T_1(I)$ Electronic Transitions in $(Et_4N)_3Fe_3F_9$ Observed in Regions I and II of Figure 5[a]

no.	energy	polarizn	temp	*f*	assignment
1b	28 713	π	28		$S = 4 \rightarrow S^* = 4$
1a	28 721	σ	1.6	1.2×10^{-8}	$S = 5 \rightarrow S^* = 4$
2b	28 063	π	7.0		$S = 4 \rightarrow S^* = 4$
2a	28 071	σ	1.6	1×10^{-9}	$S = 5 \rightarrow S^* = 4$
3b	28 097	π	7.0		$S = 4 \rightarrow S^* = 4$
3a	28 105	σ	1.6	2×10^{-9}	$S = 5 \rightarrow S^* = 4$
4b	28 145	π	7.0		$S = 4 \rightarrow S^* = 4$
4a	28 154	σ/π	1.6	1×10^{-8}/-	$S = 5 \rightarrow S^* = 4$
5b	28 154	π	7.0		$S = 4 \rightarrow S^* = 4$
5a	28 162	σ	1.6	1×10^{-8}	$S = 5 \rightarrow S^* = 4$
6	28 182	σ/π	1.6	2.4×10^{-8}	$S = 5 \rightarrow S^* = 4$
7	28 220	σ	1.6	$\approx 1 \times 10^{-7}$	$S = 5 \rightarrow S^* = 4$
8	28 290	π/σ	1.6	$\approx 2 \times 10^{-6}/\approx 7 \times 10^{-7}$	$S = 5 \rightarrow S^* = 4$
9	28 360	π/σ	1.6	$\approx 2 \times 10^{-6}/\approx 1 \times 10^{-6}$	$S = 5 \rightarrow S^* = 4$

[a] The lowest temperature at which a given transition is observed is indicated. The numbers in the first column label the Kramers doublets in the single ion. Corresponding cold and hot bands are distinguished by the indices a and b, respectively.

4.2. Optical Spectra. The positions of the maxima of the ${}^4T_1(G)$ and ${}^4T_2(G)$ bands do not differ by more than about 400 cm^{-1} in σ and π polarizations, indicating that the trigonal splittings are small. In analogy to the situation for $(Et_4N)_3Cr_2F_9$ reported in ref 27, this is due to a compression of the terminal fluoride ligands toward the metal ions, whereas the MF_3M core is elongated along the trigonal axis. Since these distortions from a perfect octahedron essentially compensate each other, the resulting trigonal energy splittings are small. However, the severe distortions from a perfect octahedron together with the electrostatic potential of the second metal ion in the dimer leads to an Fe^{3+} site with a very large odd-parity crystal-field component. This is responsible for the relatively high intensity of the principal d−d bands with ϵ values up to 5 M^{-1} cm^{-1}, see Figure 2, although all the d−d transitions in high-spin Fe^{3+} compounds are spin-forbidden and thus weak. There are two broad bands centered at 35 000 and 40 000 cm^{-1} in Figure 2, which are not expected in mononuclear Fe^{3+} complexes. In analogy with the absorption spectra of NH_4MnCl_3[31] we assign them to double excitations ${}^4T_1{}^4T_2(G)$ and ${}^4T_2{}^4T_2(G)$, respectively, since they arise at about the sums of the energies of the corresponding single excitations. These double excitations arise from exchange interactions between the Fe^{3+} ions.

4.3. The ${}^4A$, ${}^4E$ Region. There are two well-known intensity mechanisms for dimer transitions which are spin-forbidden in the single ion: (i) a single-ion mechanism due to the combined action of the odd-parity ligand field at the single ion site and spin−orbit coupling; (ii) an electric-dipole exchange mechanism. The latter, which was first proposed by Tanabe and coworkers,[18] turned out to be the most effective intensity-providing mechanism for pair transitions between states of the same single-ion electron configuration. The dimer spin selection rules for (i) are $\Delta S = 0, \pm 1$, whereas for (ii) it is $\Delta S = 0$. In the title compound the ground state levels have S values from 0 to 5, whereas the singly excited ${}^4A_1$, ${}^4E$, and ${}^4T_2(D)$ pair states have S^* values from 1 and 4. Therefore, cold bands can get intensity only from the single-ion mechanism, whereas hot bands may get intensity from both. Besides the spin selection rules, we have for the exchange mechanism the normal orbital selection rules in the C_{3h} pair symmetry:

$$A' \overset{\sigma}{\leftrightarrow} E' \qquad A'' \overset{\sigma}{\leftrightarrow} E'' \qquad A' \overset{\pi}{\leftrightarrow} A'' \tag{2}$$

On the basis of these selection rules we assign the main features in the region of the ${}^4A_1$, ${}^4E(G)$ bands shown in Figure 3 as follows. In the dimer ground state ${}^6A_1$, the $S = 0, 1, 2, 3, 4$, and 5 dimer levels transform as ${}^1A'$, ${}^3A''$, ${}^5A'$, ${}^7A''$, ${}^9A'$, and ${}^{11}A''$, respectively. The ${}^4A_1$ and ${}^4E$ singly excited pair states orbitally transform as A'/A'' and E'/E'', respectively. Pair transitions to these states can therefore only get intensity via the Tanabe mechanism in π and σ polarization, respectively. The sharp hot peak at 24 880 cm^{-1} in π polarization and the broad hot band centered at 25 150 cm^{-1} in σ polarization (Figure 3) are thus assigned to exchange-induced transitions to ${}^4A_1$ and ${}^4E$, respectively.

We do not fully understand the striking difference in the bandwidths of the ${}^4A_1$ and ${}^4E$ absorptions in Figure 3. One and perhaps the major effect is the overlap of the ${}^4E$ origins with vibrational sidebands of the ${}^4A_1$ origins. It is well-known that this often leads to a broadening of otherwise sharp features. In addition, both the ${}^4A_1$ and the ${}^4E$ excited states are further split by exchange interactions. For ${}^4A_1$ this splitting lies within the bandwidth of about 15 cm^{-1} and will be analyzed in detail in section 4.4. For ${}^4E$ this splitting is conceivably larger because, in contrast to ${}^4A_1$, the orbital occupancy within the $(t_2)^3(e)^2$ electron configuration and therefore the bonding parameters change upon ${}^6A_1 \rightarrow {}^4E$ excitation. This has two consequences: First, the relevant orbital exchange parameters and thus the energy splittings will be different from ${}^4A_1$. Furthermore, it leads to a larger displacement of the excited state potential compared

---

(31) Rodriguez, F.; Hernánez, D.; Güdel, H. U. *Phys. Rev. B* **1999**, *60*, 10598.

to the ground state potential along vibrational coordinates and therefore to longer, presumably unresolved vibrational Franck−Condon progressions. Finally, the ^{4}E state is already split into four spinor levels in the single ion. The observed broad ^{4}E absorption band is thus a superposition of a large number of unresolved sharper bands.

A number of weak, sharp features superimposed on the broad band can be identified, see Figure 3. The sidebands separated by 372, 463, and 565 cm^{-1} have the same temperature dependence as the origin in π polarization, and they are exclusively π polarized. We therefore assign them to sidebands in totally symmetric modes, forming short Franck−Condon progressions. Support for this comes from the fact that their frequencies of 372, 463, and 565 cm^{-1} are slightly higher than those of the 313, 415, and 541 cm^{-1} totally symmetric modes reported for $(Et_4N)_3Cr_2F_9$, respectively.[27] The cold 156 and 277 cm^{-1} energy sharp bands could be resolved origins of the ^{4}E pair excitations.

4.4. The $^6A_1 \rightarrow {}^4A_1$ Pair Transitions. The ground state exchange splitting is rationalized by the Heisenberg Hamiltonian in eq 1, see section 4.1. In the C_{3h} pair symmetry, the ground state pair levels transform as ^{11}A″, ^{9}A′, ^{7}A″, ^{5}A′, ^{3}A″, and ^{1}A′. The $^4A_1$ state derives from the ground electron configuration, and we can therefore use the Hamiltonian[18]

$$H' = \sum_{i,j} J_{A_iB_j} (\vec{s}_{A_i} \cdot \vec{s}_{B_j}) \qquad (3)$$

to describe the energy splitting in this excited state. In eq 3 i and j number the trigonal orbitals t_0, t_+, t_-, e_+, and e_-. Singly excited pair configurations can be represented as[23]

$$|{}^4A_1{}^6A_1\rangle \quad \text{and} \quad |{}^6A_1{}^4A_1\rangle \qquad (4)$$

Under the action of (3) they are coupled, resulting in eight pair wave functions of the general form

$$\phi_{\pm} = (1/\sqrt{2})[|{}^4A_1{}^6A_1\rangle \pm |{}^6A_1{}^4A_1\rangle] \qquad (5)$$

The excitation is delocalized between the ions A and B, leading to a resonance splitting of the levels with the same dimer spin quantum number S^*, see Figure 7. This results in two Landé patterns, a lower one with the levels transforming as ^{9}A′, ^{7}A″, ^{5}A′, and ^{3}A″ in C_{3h} and an upper one with the levels transforming as ^{9}A″, ^{7}A′, ^{5}A″, and ^{3}A′ with increasing energy. The two patterns are shown with faint and bold lines in Figure 7, respectively. Only transitions to the levels of the upper Landé pattern (bold lines in Figure 7) are symmetry allowed, and energy differences between adjacent levels are given by

$$E(S^*) - E(S^* - 1) = J_{ES}S^* \qquad (6)$$

with[18,23]

$$J_{ES} = \frac{1}{25}\left[\frac{25}{18}\sum J_{tt} + \frac{25}{24}\sum J_{ee} + \frac{25}{18}\sum J_{te}\right] \qquad (7)$$

The corresponding expression for the ground state in terms of orbital parameters is[18,23]

$$J_{GS} = \frac{1}{25}\left[\sum J_{tt} + \sum J_{ee} + 2\sum J_{te}\right] \qquad (8)$$

In eqs 7 and 8 the ΣJ_{tt}, ΣJ_{ee}, and ΣJ_{te} are the sums of 9, 4, and 12 orbital exchange parameters $J_{A_iB_j}$ defined in eq 3, respectively. In Table 3 we list the eigenvalues of eq 3 in terms of ΣJ_{tt}, ΣJ_{ee}, and ΣJ_{te}. They define the excited state splittings.

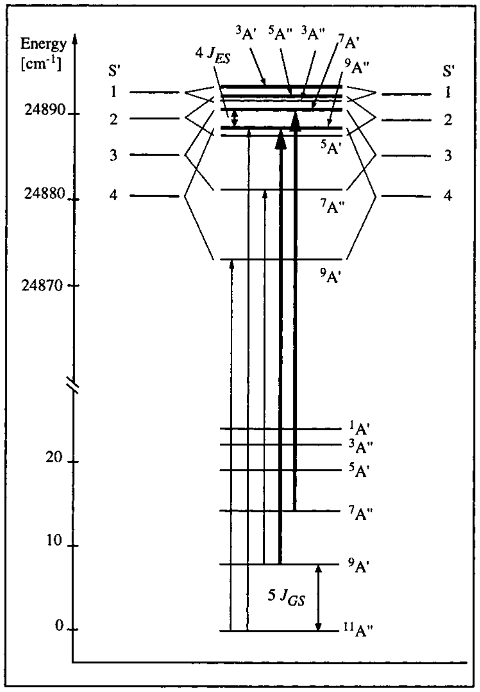

Figure 7. Energy level diagram showing the exchange splittings in the $^6A_1$ ground and the $^4A_1$ excited states. The energy levels correspond to the data analysis in section 4.4. Pair levels are labeled in C_{3h} symmetry. The arrows show the observed transitions: thick arrows indicate the spin-allowed pair transitions induced by the Tanabe mechanism, and faint arrows indicate spin-forbidden pair transitions induced by a single-ion mechanism.

Table 3. Eigenvalues of the $^4A_1$ Excited State Exchange Hamiltonian (eq 3)[a]

level	eigenvalue
$^3A_1'$	$1/1800[0\cdot\Sigma J_{tt} + 225\cdot\Sigma J_{ee} + 150\cdot\Sigma J_{te}]$
$^5A_2''$	$1/1800[200\Sigma J_{tt} + 375\cdot\Sigma J_{ee} + 350\cdot\Sigma J_{te}]$
$^7A_1'$	$1/1800[500\cdot\Sigma J_{tt} + 600\cdot\Sigma J_{ee} + 650\cdot\Sigma J_{te}]$
$^9A_2''$	$1/1800[900\cdot\Sigma J_{tt} + 900\cdot\Sigma J_{ee} + 1050\cdot\Sigma J_{te}]$
$^3A_2''$	$1/1800[-24\cdot\Sigma J_{tt} + 171\cdot\Sigma J_{ee} + 222\cdot\Sigma J_{te}]$
$^5A_1'$	$1/1800[128\cdot\Sigma J_{tt} + 213\cdot\Sigma J_{ee} + 566\cdot\Sigma J_{te}]$
$^7A_2''$	$1/1800[356\cdot\Sigma J_{tt} + 276\cdot\Sigma J_{ee} + 1082\cdot\Sigma J_{te}]$
$^9A_1'$	$1/1800[660\cdot\Sigma J_{tt} + 360\cdot\Sigma J_{ee} + 1770\cdot\Sigma J_{te}]$

[a] The parameters ΣJ_{tt}, ΣJ_{ee}, and ΣJ_{te} are the sums of 9, 4, and 12 orbital exchange parameters $J_{A_iB_j}$, respectively. The corresponding excited state dimer levels are listed on the left. The baricenter of this splitting pattern corresponds to $R(^4A_1)$, the single-ion $^4A_1$ energy.

We now assign the bands shown in Figure 4 and listed in Table 1 to distinct pair transitions. The ^{9}A′ and ^{7}A″ ground state levels lie 7.8 and 14.0 cm^{-1} above the ^{11}A″ ground level, respectively. This follows from the analysis of the magnetic susceptibility data, see section 4.1. The hot bands at 24 881 and 24 877 cm^{-1} are about an order of magnitude more intense in π than in σ polarization, see Figure 4 and Table 1, indicating that they gain their intensity mainly via the Tanabe mechanism. From their temperature dependence we conclude that they arise from the ^{9}A′ and ^{7}A″ ground state levels, respectively. On the basis of the dimer selection rules, we safely assign the bands at 24 881 and 24 877 cm^{-1} to the ^{9}A′ → ^{9}A″ and ^{7}A″ → ^{7}A′ transitions, respectively. At 1.6 K only the ^{11}A″ ground state level is populated, and transitions observed at this temperature arise from this level and necessarily gain their intensity via the single-ion mechanism. The prominent cold band at 24 873 cm^{-1}, which occurs in both polarizations, is thus immediately assigned to $^{11}A'' \rightarrow {}^9A'$. This is an important assignment, because it defines the lowest energy level of the excited state pattern in Figure 7. In both π and σ polarizations there is also hot intensity at 24 873 cm^{-1}, see Figure 4. In particular, the $^9A' \rightarrow {}^7A''$ transition is calculated at this energy. The very weak, cold band between 24 882 and 24 890 cm^{-1} is assigned to the $^{11}A'' \rightarrow {}^9A''$ transition.

With the assignments in Table 1, the J_{GS} value from the magnetic susceptibility, and the eigenvalues of eq 3 in Table 3, we are now in a position to determine the sums of orbital exchange parameters ΣJ_{tt}, ΣJ_{ee}, and ΣJ_{te}:

$$\begin{aligned} \sum J_{tt} &= +14.5 \pm 6.0\ cm^{-1} \\ \sum J_{ee} &= +6.3 \pm 5.0\ cm^{-1} \\ \sum J_{te} &= -29.8 \pm 0.7\ cm^{-1} \end{aligned} \tag{9}$$

In this analysis we also used the $^4A_1$ single-ion energy as a fit parameter and obtained $R(^4A_1) = 24\,875.9 \pm 0.2\ cm^{-1}$. We will use the parameter values for ΣJ_{tt}, ΣJ_{ee}, and ΣJ_{te} in section 5. They allow us to determine the complete excited state splitting pattern shown in Figure 7 using the eigenvalues in Table 3. It reveals that the splitting in the $^4A_1$ state is also ferromagnetic. The value $J_{ES} = -0.53\ cm^{-1}$ is obtained from the above values with eq 7. It is only a third of the ground state value $J_{GS} = -1.55\ cm^{-1}$, reflecting the observation that the $^7A'' \rightarrow {}^7A'$ transition occurs at lower energy than the $^9A' \rightarrow {}^9A''$ transition, see Figure 4 and Table 1.

4.5. The $^4T_2(D)/^2T_1(I)$ Band System. The spectra in the region of the $^4T_2(D)$ band shown in Figure 5 are essentially cold, and we thus analyze the main features in the single ion symmetry. In section 3 we have already assigned the bands in region III above 28 400 cm^{-1} to vibrational sidebands built on electronic origins located in regions I and II below 28 400 cm^{-1}. The polarizations and temperature dependencies of bands 1−6 in Figure 6 reveal that they are most likely all electronic in origin. A total of at least nine electronic transitions labeled 1−9 in Figure 5 are thus observed experimentally. The $^4T_2(D)$ single ion state is split in first order by spin−orbit coupling and the trigonal field into six Kramers doublets. This splitting is modified in the dimer, and further splittings are induced by exchange interactions. However, these latter splittings are expected to be of the same order of magnitude as in the ground and $^4A_1$ states, see sections 4.1 and 4.4, respectively, i.e., about 10−25 cm^{-1}. We have evidence of these splittings in the temperature dependence of the bands 1−6 in Figure 6 which will be discussed below. They are small compared to the splittings between the bands 1−9. We are thus forced to conclude that in addition to $^6A_1 \rightarrow {}^4T_2(D)$ another transition contributes to the spectrum in this spectral region. The bands 1−9 differ in intensity by 2−3 orders of magnitude. This suggests that the additional transition is most likely highly forbidden which gains intensity by its proximity to $^6A_1 \rightarrow {}^4T_2(D)$. We have performed an octahedral ligand field calculation using the energies of the principal bands observed in Figure 2, obtaining Racah parameter values $B = 700\ cm^{-1}$, $C = 3650\ cm^{-1}$, and a ligand-field strength of $10Dq = 12\,800\ cm^{-1}$. With these parameters we are very close to a level crossing of the $^2T_1(I)$ and $^4T_2(D)$ states at 27 850 cm^{-1}. Spin−orbit coupling splits the $^2T_1(I)$ state into three Kramers doublets which will mix with the corresponding $^4T_2(D)$ spinors. The resulting low-energy states between 27 800 and 28 200 cm^{-1} (bands 1−7 of region I in Figure 5) will thus have mixed doublet and quartet character.

Table 4. Comparison of Exchange Parameter Values (in cm^{-1}) and Metal−Metal Distances (in Å) for $(Et_4N)_3Fe_2F_9$, **1**; $CsMgCl_3{:}Mn^{2+}$, **2**, Ref 23; $CsMgBr_3{:}Mn^{2+}$, **3**, Ref 23; $Cs_3Fe_2Cl_9$, **4**, Ref 16; and $(Et_4N)_3Cr_2F_9$, **5**, Ref 27[a]

	1	2	3	4	5
J_{GS}	−1.55	+19.6	+14.2	+1.2	+27.6
J_{ES}	−0.53	+26.8	+18.6		
ΣJ_{tt}	+14.5	+490*	+355*		
ΣJ_{ee}	+6.3	0*	0*		
ΣJ_{te}	−29.8	0*	0*		
M−M	2.864	3.093	3.247	3.421	2.769

[a] Orbital exchange parameter values denoted with * were obtained by setting $\Sigma J_{ee} = \Sigma J_{te} = 0$.

We now analyze the temperature dependence of the weak bands in region I. Figure 6 shows that for each cold band 1a−5a there is a corresponding π polarized hot band 1b−5b, shifted by 7−9 cm^{-1} to the red. At 1.6 K only the lowest ground state dimer level $S = 5$ is populated; therefore the cold bands are necessarily $S = 5 \rightarrow S^* = 4$ transitions, gaining their intensity via the single ion mechanism. The hot bands are immediately increasing with temperature, and except for band 1 they are about an order of magnitude more intense than the corresponding cold bands. This strongly indicates that they gain their intensity via the exchange mechanism. We therefore assign them to $\Delta S = 0$ transitions for $S = 4$, 3, 2, and 1. The energy difference of 7−9 cm^{-1} between cold and hot absorption maxima corresponds to $5|J_{GS}|$, if the exchange splittings are the same in the ground and excited states, i.e., $J_{GS} \approx J_{ES}$. The agreement with the value $5|J_{GS}| = 7.75\ cm^{-1}$ derived from the magnetic susceptibility and the analysis of the $^4A_1$ region confirms the validity of this assumption.

In general, the intensity of the spectra shown in Figure 5 is cold, revealing that the Tanabe mechanism only plays a minor role in this band system, in contrast to the $^6A_1 \rightarrow {}^4A_1$ pair transitions, see section 4.3. This is in good accord with the theoretical prediction that the Tanabe mechanism is most efficient for pure spin−flip transitions,[18] which is the case for neither the $^4T_2(D)$ nor the $^2T_1(I)$ excitation.

5. Discussion

The most important results of our analysis are the ferromagnetic J parameters in the ground and $^4A_1$ singly excited states of $(Et_4N)_3Fe_2F_9$, **1**. This is in contrast to the situation in $CsMgCl_3{:}Mn^{2+}$, **2**, and $CsMgBr_3{:}Mn^{2+}$, **3**, in which the J parameters are antiferromagnetic in both states, see Table 4.[23] This is astonishing at first sight, since the $[Mn_2X_9]^{5-}$ pairs in **2** and **3** have the same bridging geometry as the $[Fe_2F_9]^{3-}$ pairs in **1**, and they are isoelectronic. This difference can be rationalized on the basis of the relevant orbital exchange parameters listed in Table 4. The $J_{A_iB_j}$ parameters belonging to overlapping orbitals can provide antiferromagnetic, i.e., positive contributions to J_{GS} and J_{ES}. Overlap in the present trigonal symmetry is restricted to the parameters $J_{t_0t_0}$, $J_{t_+t_+}$, and $J_{t_-t_-}$ in ΣJ_{tt}, $J_{e_+e_+}$ and $J_{e_-e_-}$ in ΣJ_{ee}, and $J_{t_+e_+}$, $J_{e_+t_+}$, $J_{t_-e_-}$, and $J_{e_-t_-}$ in ΣJ_{te}. All the other 16 orbital parameters are necessarily negative.

In trigonal dimers composed of two face-sharing octahedra, the interaction between the t_0 orbitals leads to the main antiferromagnetic contribution, since they are directly pointing toward each other. This was nicely borne out in various studies on triply bridged Cr^{3+} dimers[32−34] and was also found for **2**

---

(32) Leuenberger, B.; Güdel, H. U. *Inorg. Chem.* **1986**, *25*, 181.
(33) Schenker, R.; Weihe, H.; Güdel, H. U. *Inorg. Chem.* **1999**, *38*, 5593.
(34) Niemann, A.; Bossek, U.; Wieghardt, K.; Butzlaff, C.; Trautwein, A. X.; Nuber, B. *Angew. Chem., Int. Ed. Engl.* **1992**, *31*, 311.

and **3**:[23] The ratios of J_{ES}/J_{GS} are 1.37 and 1.31 in **2** and **3**, respectively. These values are very close to the value of 1.39 obtained from eqs 7 and 8 when $\Sigma J_{ee} = \Sigma J_{te} = 0$, indicating that ΣJ_{tt} is by far the dominant term for **2** and **3**. Consequently, in these dimers the splittings are antiferromagnetic in both the ground and the $^4A_1$ excited state as a result of the dominant $J_{t_0t_0}$ parameter. A decrease of the metal−metal separation leads to an increased overlap of the t_0 orbitals and thus to an increase of the antiferromagnetic splittings.[34,35] This is also observed for **2** and **3**, where both J_{GS} and J_{ES} increase from 14.2 and 18.6 cm^{-1} in the bromide to 19.6 and 26.8 cm^{-1} in the chloride, respectively, upon decreasing the Mn−Mn distance from 3.247 to 3.093 Å, see Table 4. Because of the considerably shorter Fe−Fe distance of 2.864 Å, an even larger antiferromagnetic exchange might be expected for **1**. However, we observe a decrease instead. This is due to the additional positive charge on Fe^{3+} compared to Mn^{2+}, leading to a strong radial contraction of the orbitals in Fe^{3+} and therefore to a considerable reduction of all the orbital overlap and electron-transfer integrals. As a direct consequence, ΣJ_{tt} is decreased from 490 and 355 cm^{-1} in **2** and **3** to 14.5 cm^{-1} in **1**, respectively, i.e., by more than 1 order of magnitude, see Table 4. This effect is also illustrated by a comparison of the d^3 systems $CsMgCl_3$:V^{2+} containing $[V_2Cl_9]^{5-}$ pairs[36] and $Cs_3Cr_2Cl_9$,[37] in both of which $J_{t_0t_0}$ provides the major contribution to the antiferromagnetic ground state exchange parameter J_{GS}. J_{GS} is decreased from 187 to 13 cm^{-1}, respectively, despite the similar metal−metal separations of 3.09 and 3.12 Å, respectively.[36,37] We conclude that the relevant overlap and electron-transfer integrals are much more influenced by changes of the metal charges than by changes of the metal−metal separation. In **1** the antiferromagnetic pathway via the direct overlap of the t_0 orbitals has clearly lost its dominance. ΣJ_{ee} and ΣJ_{te}, which could be neglected in **2** and **3** due to the dominance of ΣJ_{tt}, now become important in **1**. The dominant term in **1** is $\Sigma J_{te} = -29.8$ cm^{-1}, giving rise to the observed ferromagnetic splittings in both the ground and $^4A_1$ excited states. The negative value for ΣJ_{te} reflects the fact that it is composed of 12 orbital parameters, 8 of which are necessarily ferromagnetic.

For $Cs_3Fe_2Cl_9$, **4**, a value of $J_{GS} = 1.2$ cm^{-1} was reported.[16] The ground state splitting thus changes from ferromagnetic in **1** to antiferromagnetic in **4**. The decrease of the t_0 orbital overlap and thus $J_{t_0t_0}$ due to the strong enlargement of the Fe−Fe distance from 2.864 to 3.421 Å must therefore be overcompensated by increased antiferromagnetic contributions of pathways involving the ligands, leading to increased positive values of the terms J_{t+t+} and J_{t-t-} in ΣJ_{tt} and J_{e+e+} and J_{e-e-} in ΣJ_{ee}. Physically this corresponds to a better overlap of metal and ligand orbitals, which is due to the increased covalency of the Fe−Cl compared to the Fe−F bonds. But we note that $J_{GS} = 1.2$ cm^{-1} in $Cs_3Fe_2Cl_9$ is very small, indicating a very fine balance between ferromagnetic and antiferromagnetic contributions. Finally, we can compare the results of $(Et_4N)_3Fe_2F_9$, **1**, with those reported recently for the tri-fluoro bridged Cr^{3+} dimer $(Et_4N)_3Cr_2F_9$, **5**.[27] In the latter the ground state splitting is antiferromagnetic with $J_{GS} = +27.6$ cm^{-1}, and the Cr−Cr distance is 2.769 Å, see Table 4. This considerably shorter metal−metal distance than in the title compound (2.864 Å) will lead to a larger positive $J_{t_0t_0}$ and therefore ΣJ_{tt} in $(Et_4N)_3Cr_2F_9$. In addition there are no ferromagnetic contributions from ΣJ_{te}, since Cr^{3+} has a $(t_2)^3$ electron configuration.

In conclusion, we have presented single-crystal magnetic susceptibility data and high-resolution crystal absorption spectra of $(Et_4N)_3Fe_2F_9$ at cryogenic temperatures. This allowed us to determine exchange splittings and exchange parameters in the ground and $^4A_1$ excited states. They were both found to be ferromagnetic, which is in contrast to the situation in the analogous $[Mn_2X_9]^{5-}$ pairs in $CsMgX_3$:Mn^{2+} ($X = Cl^-$, Br^-). This was rationalized on the basis of orbital exchange parameters derived from the spectra. We find that in the $[Fe_2F_9]^{3-}$ and $[Fe_2Cl_9]^{3-}$ dimers all of the relevant overlap and electron transfer integrals are strongly reduced compared to the corresponding Mn^{2+} dimers. This is the result of a strong radial contraction of the d orbitals in Fe^{3+} due to the increased positive charge of the nucleus. The antiferromagnetic pathway via the t_0 orbitals is therefore no longer dominant, and positive and negative orbital parameters become similar in magnitude. This results in small net exchange splittings in $[Fe_2X_9]^{3-}$ ($X = F^-$, Cl^-), which are ferromagnetic or antiferromagnetic depending on the Fe−Fe distance and the covalency of the Fe−ligand bonds. The difference between $(Et_4N)_3Fe_2F_9$ and $Cs_3Fe_2Cl_9$ reveals that, although weak, the interactions via the bridging ligands give the crucial contribution to the net exchange. This is substantially different from the situation in $CsMgX_3$:Mn^{2+} ($X = Cl^-$, Br^-) and $(Et_4N)_3Cr_2F_9$, in which the antiferromagnetic orbital parameter $J_{t_0t_0}$ dominates the picture.

Acknowledgment. We thank Karl Krämer for performing the X-ray powder diffractograms and the Rietveld analysis. Financial support from the Swiss National Science Foundation and the European Science Foundation is gratefully acknowledged.

IC010129P

---

(35) Grey, I. E.; Smith, P. W. *Aust. J. Chem.* **1971**, *24*, 73.
(36) Riesen, H.; Güdel, H. U. *Inorg. Chem.* **1984**, *23*, 1880.
(37) Briat, B.; Russel, M. F.; Rivoal, J. C.; Chapelle, J. P.; Kahn, O. *Mol. Phys.* **1977**, *34*, 1357.